Ionics (2022) 28:4719–4728
https://doi.org/10.1007/s11581-022-04702-4

ORIGINAL PAPER

Fe, P, N, S multidoping porous graphene material as a Bifunctional OER/ORR electrocatalytic activity for enhancing rechargeable Zn-air batteries

Dukhyun Nam[1] · **Jooheon Kim**[1,2,3]

Received: 25 April 2022 / Revised: 10 July 2022 / Accepted: 26 July 2022 / Published online: 2 August 2022

Abstract

Oxygen evolution reaction (OER) and oxygen reduction reaction (ORR) electrocatalyst activity may be regarded as a crucial indicator of expected performance in metal-air batteries, which are limited by the inadequate electrochemical activity and low conductivity of accessible materials. This disadvantage can be solved by the development of hierarchically structured three-dimensional (3D) carbon. Through carbonization method, we synthesize the bifunctional catalysts, Fe, P, N, and S multidoped porous graphene (FePNS-G) for use in rechargeable Zn–air batteries (ZABs). FePNS-G-2 indicates superior active site density for both the OER and ORR. Moreover, the FePNS-G-2 exhibits excellent long-term electrochemical stability for 10 h in both the OER and ORR. ZABs assembled for FePNS-G-2 shows a higher power density (168.3 mW cm^{-2}) and a higher specific capacity (782.36 mA h g^{-1}) than benchmark Pt/C + IrO_2 electrocatalyst. The sturdy durability of FePNS-G-2 for OER and ORR leads to the charge–discharge cycle durability. The excellent electrocatalytic activity and steady cycling life of FePNS-G-2 examines the air cathode as an electrocatalyst in feasible ZAB applications.

Keywords Graphene · Hierarchical porous carbon · Oxygen evolution reaction · Oxygen reduction reaction · Zn-air battery

Introduction

These days, increasing energy demand and traditional fossil fuel problems have forced us to use ecofriendly storage systems and energy conversion [1–3]. Among these techniques, the Zn-air batteries (ZABs) are evaluated as a suitable energy storage system for the next-generation due to its safety and high energy density of 1084 Wh kg^{-1} [3–11]. But, the sluggish oxygen reduction reaction (ORR) which are the discharge reaction in the air electrode and oxygen evolution reaction (OER) which are the charge reaction in the air electrode activity decline the energy efficiency of ZABs [12]. For this battery to work in common devices, it is important to develop high-performance bifunctional electrocatalysts for OER and ORR. Much research has been performed to progress extremely steady materials and active site for an air cathode [13, 14]. Generally, Ir-based and Pt-based catalysts are used electrocatalysts for OER and ORR, respectively [15]. However, the low activity of the Ir-based materials for ORR and the moderate activity of the Pt-based materials for OER hinder use alone in Zn-air batteries [16–22]. Therefore, the research efforts to replace the precious metal catalyst of rechargeable Zn-air battery using a high-performance, cost-effective, and easily prepared non-precious metal bifunctional oxygen electrocatalyst. When conducting study on noble metal-free catalysts, the carbon materials such graphene and carbon nanotube have been extensively studied because of their high surface area and excellent electric conductivity [23–27]. However, the performance of the electrocatalyst of the carbon materials is dissatisfying. Because of the variations in the electronegativity, bonding state, and atom size of heteroatoms, carbon doped with different heteroatoms displays different catalytic properties [28–33]. Single heteroatom-doped

✉ Jooheon Kim
jooheonkim@cau.ac.kr

[1] School of Chemical Engineering & Materials Science, Chung-Ang University, 84 Heukseok-ro, Dongjak-gu, Seoul, Korea

[2] Department of Advanced Materials Engineering, Chung-Ang University, Anseong-si, Gyeonggi-do 17546, Republic of Korea

[3] Department of Intelligent Energy and Industry, Graduate School, Chung-Ang University, Seoul 06974, Republic of Korea

carbon generally indicates electrocatalytic activity fair for ORR and OER reactions [34, 35]. For instance, Tian et al. studied that nitrogen-doped carbon-coated carbon nanotubes (CNTs) were efficient catalysts for OER and ORR [36]. In addition, Alekha Tyagi et al. studied that the piperazine with covalent triazine framework (P-CTF) nanoflowers assembled from the nanosheets were synthesized through ultrasound-triggered way [37]. Therefore, carbon with a large amount of heteroatom doping is a crucial strategy for realizing a multifunctional catalyst with enhanced catalytic performance. For example, the co-doped graphitic sheets of S and N might catalyze OER and ORR reactions at the same time [38–40]. Besides, the Fe doping aids in the production of OER activity [41]. Even though there are related studies on heteroatom-doped carbon materials that catalyze these two reactions, the catalyst performance is dissatisfactory. But the bifunctional catalysts could simplify the electrode design and prevent side effects caused by interaction of different catalysts. Heteroatom doping and vacancy engineering can increase the electrical activity of nanocarbon materials, but these can be accompanied by side effects, especially a decrease in electrical conductivity. Hybridization of diverse carbon nanostructures supplies the more active site and the proactive method to further enhance electrocatalyst performance through various effects such as increasing electrical conductivity [42]. For example, the ultratanin N-doped hollycarbon layers (HLCs) were grown on graphene nanosheets (NHC@G) to supply rich active sites without ruining the sp^2 conjugate structure [43]. Therefore, it is critical to develop an activated bifunctional carbon-based electrocatalysts for both reactions. It has been notified that the spin density and charge density of atoms influence electrochemical reduction activity toward oxygen. The difference in electronegativity between N-P and N-S is 2.19 and 2.58, respectively, resulting in spin density change [44, 45]. So, the doping of atom breaks the electronegativity of graphene and produces a charged part, thereby helping to improve electrochemical conductivity as well as adsorption capacity. Whereas the small amounts of metals doped into the sp^2 carbon skeleton supplied extra improvements to electrocatalyst properties of the materials [44, 46]. To use their application efficiently, the active sites should be made as easily as possible in the materials, which can be reinforced by optimized dimensionality and porosity. The open pore 3D system provides pore and channels networks of electrodes, supporting to enhance charge and mass transfer [47, 48]. In this work, we demonstrate Fe, P, N, and S multidoped porous graphene materials (FePNS-G) into carbon materials. FePNS-G with activity sites (Fe, P, N, and S co-doped carbon), porous structure, and high surface area accomplishes excellent bifunctional activities. The rechargeable ZABs assembled with FePNS-G-2 indicate a specific capacity (782.36 mA h g^{-1}) and high-power density (168.3 mW cm^{-2}). Moreover, the initial charge–discharge voltage gap of FePNS-G-2 is lower than benchmark Pt/C + IrO_2.

Experimental method

Materials

Tetraphenylphosphonium bromide ($C_{24}H_{20}P(Br)$) and ammonium persulfate were purchased from Sigma-Aldrich and Alfa Aesar, respectively. And iron nitrate nonahydrate was purchased from Daejung. Ethanol and 1 M hydrochloric acid (HCl) were purchased form Daejung and Samchun Chemicals.

Synthesis of Fe, P, N, and S multidoped porous graphene

The porous graphene doped with Fe, P, N, and S was synthesized by carbonization process. In this process, tetraphenylphosphonium bromide ($C_{24}H_{20}P(Br)$) was introduced as carbon and phosphorus source, and ammonium persulfate ($(NH_4)_2S_2O_8$) was introduced as sulfur and nitrogen precursor, and iron nitrate nonahydrate ($Fe(NO_3)_3 \bullet 9H_2O$) as iron source. In a common experiment, firstly, 0.419 g $C_{24}H_{20}P(Br)$ was sonicated in 0.4 mL ethanol and then the 6 mL of 1 M aqueous HCl was mixed together under stirring for 15 min. After stirring, 1.37 g $(NH_4)_2S_2O_8$ was added to the mixed solution and then stirred for 15 min. After stirring, 0.404 g $Fe(NO_3)_3 \bullet 9H_2O$ was added into the above mixed solution. Then, the mixture was transferred to a 10-mL vial. And then, to remove the impurity, the obtained precipitate was centrifuged and separated with ethanol several times. The product was frozen and dried for overnight. Finally, the dried powder was annealed to 1000 °C at a heating rate of 5 °C min^{-1} and maintained for 2 h under N_2 atmosphere. The resulting sample was written in FePNS-G-1. The Fe doping amount of graphene was controlled to the mass ratio of $Fe(NO_3)_3 \bullet 9H_2O$ to $(NH_4)_2S_2O_8$ and $C_{24}H_{20}P(Br)$. Under the same condition, The samples synthesized with 0.808 g and 1.212 g $Fe(NO_3)_3 \bullet 9H_2O$ were controlled with FePNS-G-2 and FePNS-G-3, respectively (Table 1).

Table 1 Comparison of solution resistance (R_s) and charge transfer resistance (R_{ct}) for OER and ORR

Sample	OER		ORR	
	R_s (Ω)	R_{ct} (Ω)	R_s (Ω)	R_{ct} (Ω)
FePNS-G-1	11.93	61.25	46.37	732.23
FePNS-G-2	13.29	18.26	46.12	796.93
FePNS-G-3	13.94	27.97	46.19	953.81

Material characterization

The morphology of FePNS-G-1, FePNS-G-2, and FePNS-G-3 was confirmed by field-emission scanning electron microscopy (FE-SEM, SIGMA 300/Carl Zeiss) and field-emission transmission electron microscopy (FE-TEM, JEM-F200/JEOL) equipped with the energy dispersive spectrometer (EDS). To confirm crystal structures of materials of samples, X-ray diffraction (XRD, New D8-Advance/Bruker-AXS) patterns were collected at a scan rate of 1° s^{-1} within the 2 θ range of 10–80 using Cu K α_1 radiation (0.1540 nm). Raman spectroscopy was performed by DXR2xi, Thermo, USA with a 514-nm argon laser (power: 1 mW). Nitrogen adsorption analysis was performed by using an ASAP 2020 accelerated surface area and porosity measuring instruments with automated surface area at 77 K using Brunauer–Emmett–Teller (BET) calculations for the surface area. To analyze elemental bonding, the X-ray photoelectron spectroscopy (XPS, K-alpha + /ThermoFisher Scientific) was used.

Zn-air battery test

The performance of a liquid rechargeable Zn-air batteries was explored by manufacturing it with various four catalysts. An air cathode containing FePNS-G-2 as the catalyst was manufactured as follows: FePNS-G-2 (0.005 g) was dispersed with an aqueous Nafion solution (0.001 L, 0.5wt%) under sonication, and the as-prepared mixture was uniformly coated on a piece of carbon paper (HCP030) until catalyst loading of 1 mg/cm^2. As an air cathode and an anode of a Zn-air batteries, carbon paper coated with FePNS-G-2 and a polished Zn plate were used, respectively. As an electrolyte a KOH solution (6 M) + zinc acetate (0.2 M) was used. Likewise, a mixture of Pt/C + IrO_2 (1:1) was coated on a carbon paper to prepare the corresponding air–cathode.

At room temperature, the performance of assembled Zn-air batteries connected to electrochemical workstation (CS350) device was performed. The charge and discharge polarization curves were acquired through LSV measurement at a scan rate of 10 mV/s. To establish the specific capacitance, galvanostatic discharge was performed until the entire Zn plate was consumed at a current density of 10 mA/cm^2. The specific capacitance was calculated using Eq. (1):

$$\text{Specific capacitance (mAh/g)} = \text{I} \times \frac{t}{W_{Zn}} \quad (1)$$

where I, t, and W_{Zn} are the current, testing time, and zinc consumption, respectively. The galvanostatic discharge–charge cycle test was conducted at a current density of 10 mV/s at a time of 5 min for discharging and charging.

Results and discussion

Synthesis, morphology, and structure of FePNS-G-2

The synthetic of Fe, P, N, and S multidoped porous graphene (FePNS-G) by carbonization was indicated in Fig. 1a. First, we synthesized $C_{24}H_{20}P(Br)$ by mixing ethanol and HCl using an easy method. After adding $Fe(NO_3)_3 \bullet 9H_2O$, we annealed to 1000 °C under N_2 atmosphere and then obtained Fe, P, N, and S multidoped porous graphene. To examine the morphology of the as-prepared catalysts, the image of FePNS-G surfaces was obtained by FE-SEM and FE-TEM in Fig. 1b–e, and Figs. S1–S4. Both structures consisted of the ultrathin porous nanosheets [44]. Uniform spaces appearing in the images bring about the HCl template. When used as air cathodes, the electrodes with voids can be useful in mass transport points and electron transfer of view, which is useful for improving OER and ORR performance [49]. Their loose structures could be seen in FE-TEM images shown in Fig. 1d–e, and Figs. S3–S4 due to formation such as bubbles with a diameter of less than 100 nm connected. It can be concluded that the image of FE-TEM confirms the porous structure. Moreover, to investigate the atomic distribution, EDS was performed. As shown in Fig. 1g, The Fe, P, N, S, and C species were evenly spread to the as-obtained sample.

To analyze the crystal structures of materials, X-ray diffraction (XRD) was carried out in Fig. 2a and Fig. S11. According to previous reports [38], the XRD pattern of all catalysts show only one (0 0 2) peak at 25° the carbon phase, suggesting the amorphous state of the FePNS-G-1, FePNS-G-2, and FePNS-G-3 sample. Also, according to previous reports [50], it is found that it was $C_{24}H_{20}P(Br)$. Furthermore, to study the influence of defect in the carbon structure, Raman spectroscopy was conducted in Fig. 2b. The as-prepared catalysts showed two distinct peaks at about 1349 cm^{-1} and 1582 cm^{-1}, which were consistent with D-band of the messy carbon with faulty sites and G-band for showing graphite side, respectively. The I_D/I_G ratio value is 1.26, 1.43, and 1.38 for FePNS-G-1, FePNS-G-2, and FePNS-G-3, respectively. The increased I_D/I_G shows an increase in the structural defects and indicates a gradually increased level of heteroatom doping [51]. These results implies that more deficiencies were established to the carbon materials. This deficiency-rich carbon displayed great catalysis activities for OER and ORR. To investigate the porous structure and surface area of all samples, the N_2 adsorption–desorption isotherms were conducted. The Brunsuer-Emmett-Teller (BET) surface area of FePNS-G-2 is 370.96 $m^2\ g^{-1}$, which is the higher than those of FePNS-G-1 (99.21 $m^2\ g^{-1}$) and FePNS-G-3 (270.53 $m^2\ g^{-1}$) in Fig. 2c. The highly formed porous structure in FePNS-G-2 can help mass transport for OER and ORR [38].

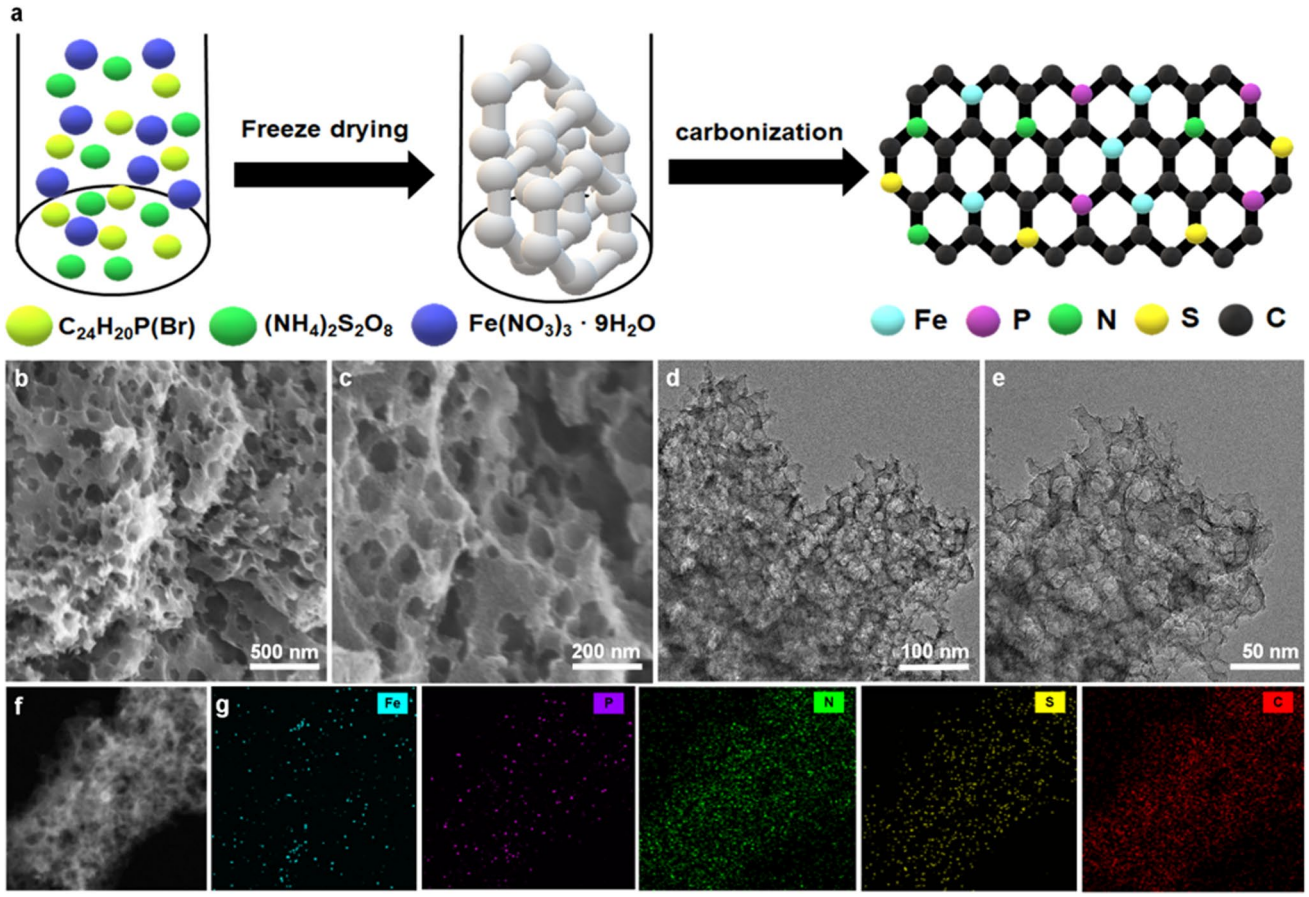

Fig. 1 **a** Schematic illustration of synthetic methods. **b** Low magnification FE-SEM image of FePNS-G-2. **c** High magnification FE-SEM image of FePNS-G-2. **d** Low magnification FE-TEM image of FePNS-G-2. **e** high magnification FE-TEM image of FePNS-G-2. **f** Dark-field TEM image of FePNS-G-2. **g** EDS mapping of FePNS-G-2

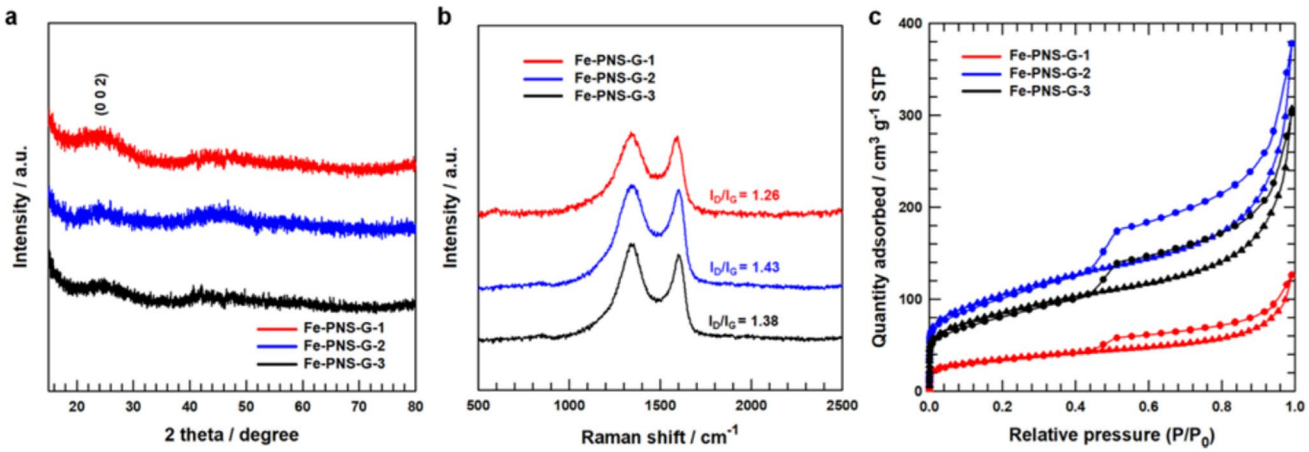

Fig. 2 **a** XRD patterns of FePNS-G-1, FePNS-G-2, and FePNS-G-3. **b** Raman spectra of FePNS-G-1, FePNS-G-2, and FePNS-G-3. **c** N2 adsorption–desorption isotherms of FePNS-G-1, FePNS-G-2, and FePNS-G-3

To confirm the elemental valence and composition of the as-prepared catalysts, XPS was performed in Fig. 3. As shown in Fig. 3a, the XPS survey spectra were displayed by contrasting FePNS-G-1, FePNS-G-2, and FePNS-G-3. FePNS-G-1, FePNS-G-2, and FePNS-G-3 had four peaks of Fe, P, N, S, and C elements. The Fe 2p spectra of

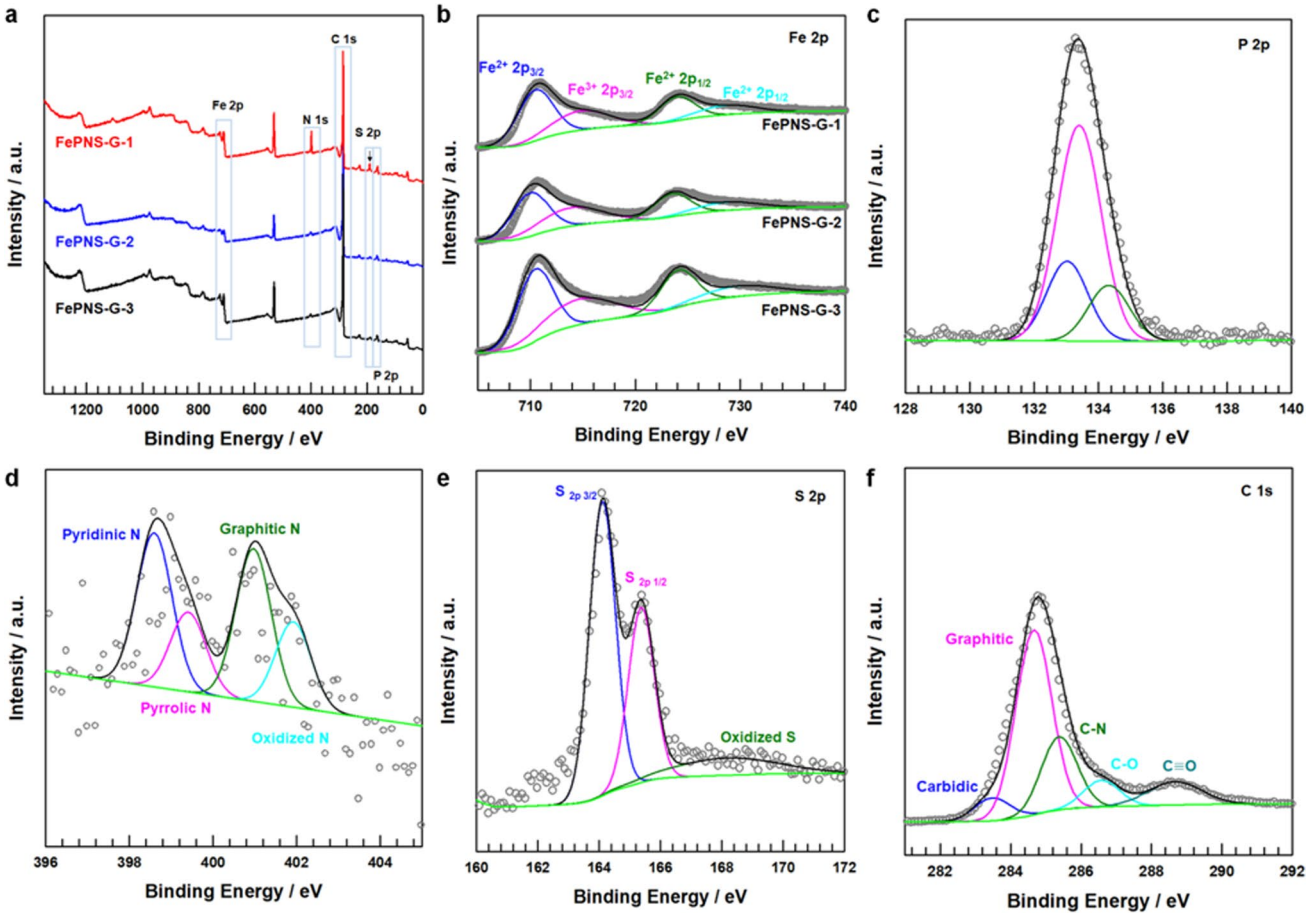

Fig. 3 **a** XRS survey of FePNS-G-1, FePNS-G-2, and FePNS-G-3. **b** XPS Fe 2p deconvolution spectra of FePNS-G-1, FePNS-G-2, and FePNS-G-3. **c** XPS N 1 s deconvolution spectra of FePNS-G-2. **d** XPS P 2p deconvolution spectra of FePNS-G-2. **e** XPS S 2p deconvolution spectra of FePNS-G-2. **f** XPS C 1 s deconvolution spectra of FePNS-G-2

FePNS-G-1, FePNS-G-2, and FePNS-G-3 were displayed in Fig. 3b. As previously reported [52], the Fe 2p spectra indicated four fitting of Fe species in FePNS-G-1, FePNS-G-2, and FePNS-G-3, corresponding to Fe^{2+} 2p $_{3/2}$ (710.46, 710.38, and 710.42 eV), Fe^{3+} 2p $_{3/2}$ (714.78, 714.23, and 714.5 eV), Fe^{2+} 2p $_{1/2}$ (723.92, 723.89, and 723.9 eV), and Fe^{3+} 2p $_{1/2}$ (728.68, 728.23, and 729.17 eV), respectively. The iron contents were very low so Fe cannot discover by XRD for all samples. On the contrary, there is a negative change corresponding to the Fe 2p spectra of FePNS-G-2 compared to FePNS-G-1 and FePNS-G-3. The results indicate the bonding effect between Fe 2p and N 1 s in FePNS-G samples. According to previous report [52], the rich Fe^{2+} species in FePNS-G-2 can play a main role in outstanding ORR active site since Fe2 + −N4 can play the role of the active sites. For P 2p spectra of FePNS-G-2 (Fig. 3c), the P 2p spectrum showed three fitting of P 2p in FePNS-G-2, corresponding to P–C (133 eV), P-N (133.5 eV), and P-O (134.3 eV), respectively [53]. Figure 3d indicates the N 1 s spectra of FePNS-G-2 peak can be divided four peaks located in pyridinic N (398.59 eV), pyrrolic N (399.4 eV), graphitic N (400.9 eV), and oxidized N (401.92 eV), respectively [53]. As shown in Fig. 3e, the S 2p spectrum of FePNS-G-2 displayed three peaks, corresponding to S 2p $_{3/2}$ (164.1 eV), S 2p $_{1/2}$ (165.37 eV), and oxidized S (168.16 eV), respectively [53]. The C 1 s regions of FePNS-G-2 were indicated in Fig. 3f. Carbon substrate defects are identified by showing peak for carbidic, graphitic, C-N, C-O, and C ≡ O bonding [44]. The existence of C-N can be considered evidence of accomplished N doped into C network which proved by N incorporation into sp^2 orbital proven from its 1 s spectrum [44].

Oxygen electrochemical performance of electrocatalysts

To estimate the activity sites for OER and ORR, the three-electrode configurations with a working electrode, a counter electrode, and a reference electrode was used for N_2-saturated 1 M KOH and O_2-saturated 0.1 M KOH for

OER and ORR, respectively. OER is charge reaction generated by the air cathode of the Zn-air batteries. Linear sweep voltammetry (LSV) curves were obtained to evaluate the activity site of all prepared samples in Fig. 4a. This FePNS-G-2 displayed better catalytic activities than other catalysts. To investigate the kinetic activity of catalysts, Tafel slopes were calculated through LSV in Fig. 4b. FePNS-G-2 indicated lower Tafel slope than those of FePNS-G-1 and FePNS-G-3. These displayed that the Fe content had a great effect on the electrochemical performance of the samples, and a reasonable degree of doping optimize the OER kinetics [54]. To verify the OER kinetics of all prepared catalysts, electrochemical impedance spectroscopy (EIS) was performed in Fig. 4c. The circuit consisted of charge-transfer resistance (R_{ct}) and solution resistance (R_s). FePNS-G-2 displayed the smallest R_{ct}, suggesting improved charge-transfer between the electrode and electrolyte and corresponding to the above results. Before the OER test, the electrochemical double-layer capacitance (C_{dl}) was calculated since the surface area of catalysts is an important factor for catalytic activity. C_{dl} was calculated by cyclic voltammetry (CV) at a non-faradaic region in Fig. 4d and Fig. S5. Besides, stability is also critical factor for OER. To analyze the stability of electrocatalysts, LSV curves were performed before and after 2000 cycles for both FePNS-G-2 and commercial IrO_2 in Fig. 4e. Fe-PNS-G-2 displayed a little decline after the 2000 cycles. However, benchmark IrO_2 indicated considerably decline after the 2000 cycles. Besides, chronoamperometry (CA) measurements were performed in Fig. 4f. The FePNS-G-2 catalyst showed little decrease 89.18% after a 10-h CA measurement, suggesting excellent electrocatalytic stability at 1.62 V. The stability result shows that Fe-NPS-G-2 are favorable OER catalyst.

A rotating ring disk electrode (RRDE) system was used to analyze the ORR performance. LSV was performed using RRDE to investigate the activity, and the results are shown in Fig. 5a, c and Fig. S7. FePNS-G-2 indicated higher half-wave potential than the other catalysts. As previously described, higher ORR activity might be attributed to higher graphitization in FePNS-G-2, which helped electron

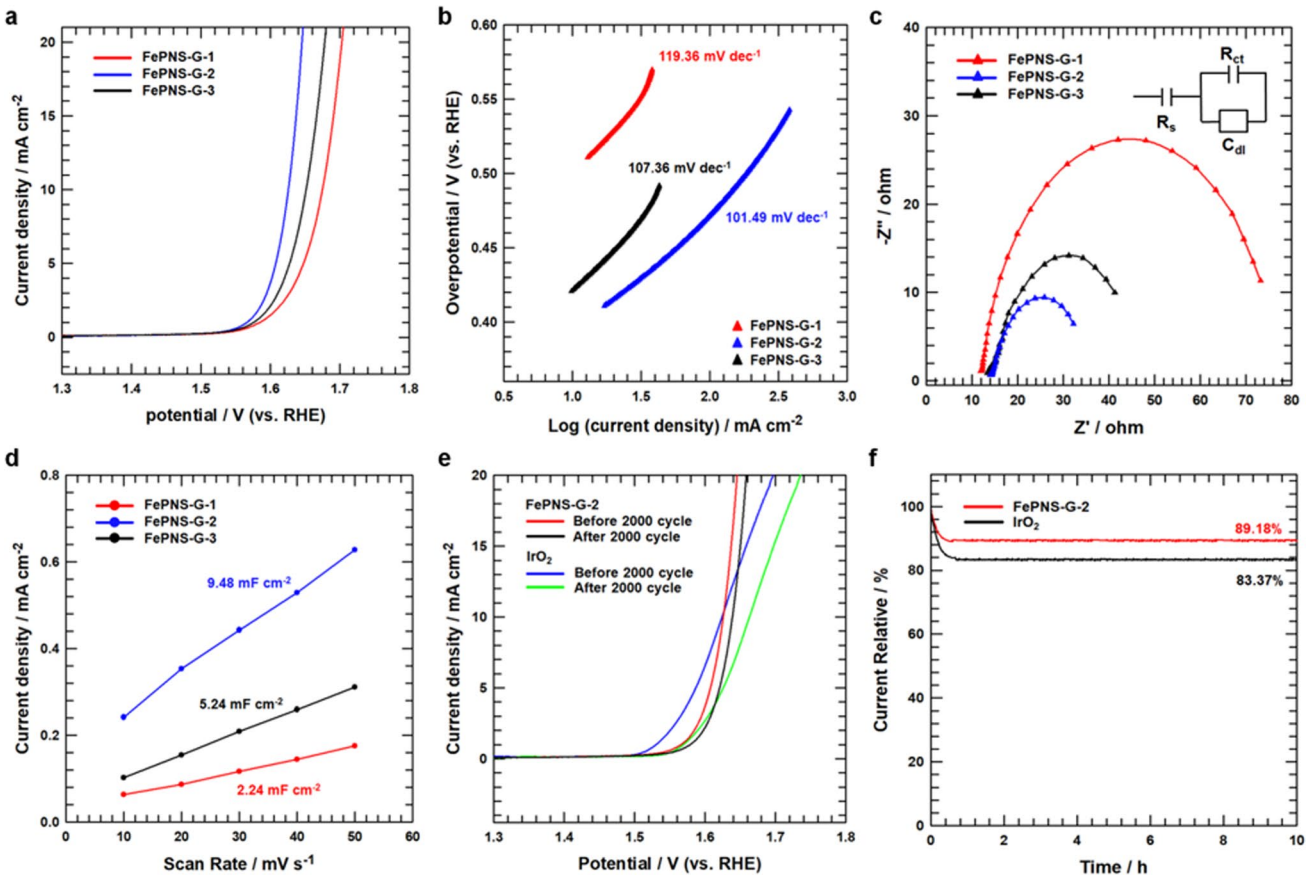

Fig. 4 **a** OER RDE LSV curves for FePNS-G-1, FePNS-G-2, and FePNS-G-3. **b** Tafel plots for FePNS-G-1, FePNS-G-2, and FePNS-G-3 at OER potential. **c** Nyquist plots FePNS-G-1, FePNS-G-2, and FePNS-G-3 at OER potential **d** linear fitting of the capacitive currents versus CV scan rates of FePNS-G-1, FePNS-G-2, and FePNS-G-3. **e** OER LSV curves for before and after 2000 CV cycles FePNS-G-2 and IrO2. **f** Chronoamperometry for FePNS-G-2 and IrO2 at OER potential

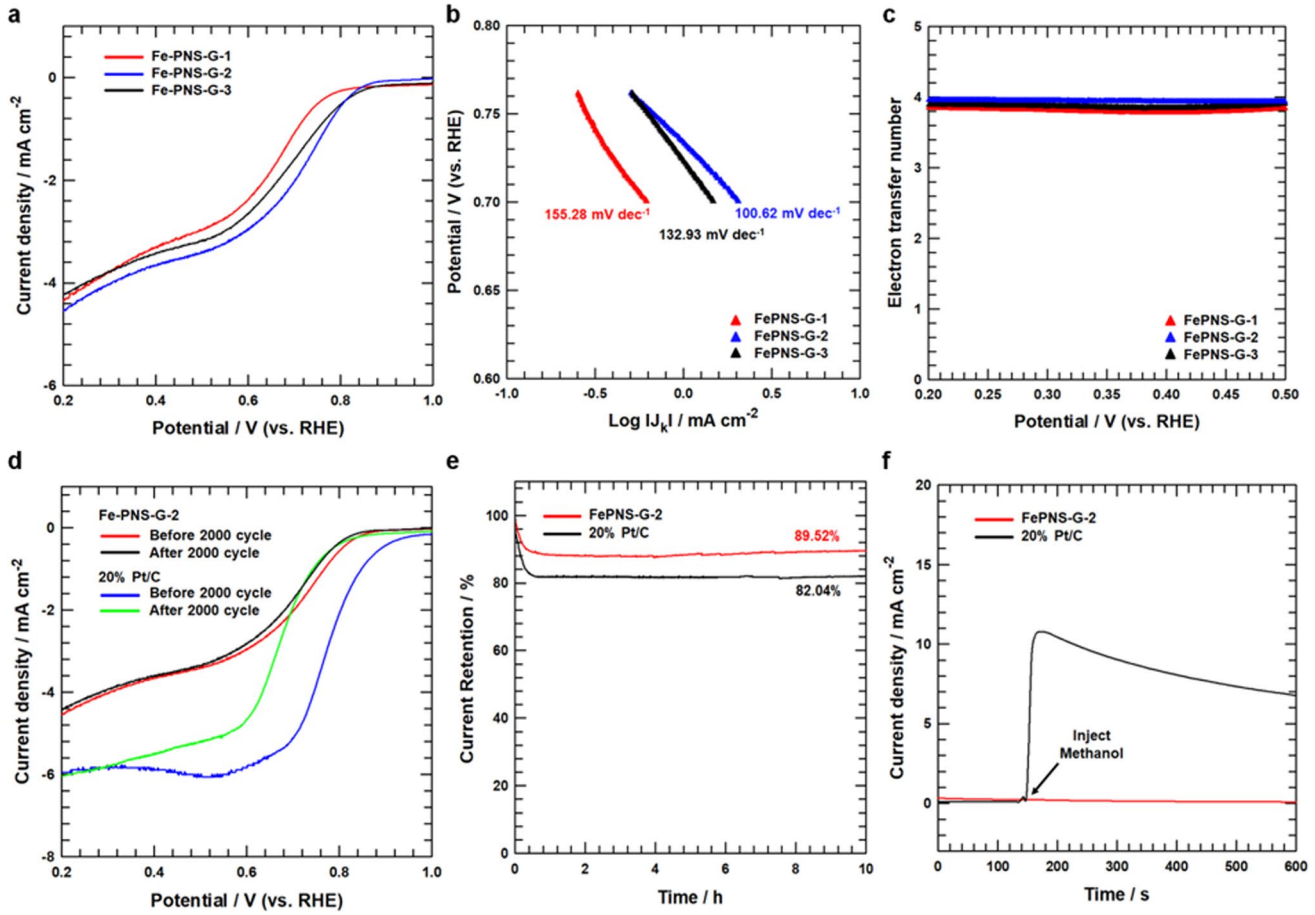

Fig. 5 **a** ORR RRDE LSV curves for FePNS-G-1, FePNS-G-2, and FePNS-G-3. **b** Tafel slope for FePNS-G-1, FePNS-G-2, and FePNS-G-3 at ORR potential. **c** Electron transfer number for FePNS-G-1, FePNS-G-2, and FePNS-G-3. **d** ORR LSV curves for before and after 2000 CV cycles FePNS-G-2 and Pt/C. **e** Chronoamperometry for FePNS-G-2 and Pt/C at ORR potential. **f** Methanol tolerance test of FePNS-G-2 and Pt/C

transport, optimum dispersed Fe content, increasing the ratio of Fe to adjusted N to the total Fe content, and improved access to catalyst sites [55]. To analyze the intrinsic active sites of catalysts for ORR, Tafel slopes were calculated through Tafel plot in Fig. 5b. ORR current consisted of two parts: diffusion current and kinetic current. Tafel plot was calculated using kinetic current to indicate the intrinsic activity for ORR in Fig. 5b. FePNS-G-2 showed lower Tafel slope than those of FePNS-G-1 and FePNS-G-3, suggesting the highest ORR kinetics. Through Fig. 5a and Fig. S6, by equations in electrochemical measurements, the electron transfer number and peroxide (H_2O_2) yield for ORR are calculated in Fig. 5c and Fig. S7. The electron transfer number of FePNS-G-2 was nearly 4, confirming the ideal ORR mechanism. Since the H_2O_2 yield of FePNS-G-2 was smaller than FePNS-G-1 and FePNS-G-3, suggesting these excellent achievements could be attributed to many defective carbon materials. EIS was performed for ORR in Fig. S8. FePNS-G-2 was the smaller R_{ct} than FePNS-G-1 and FePNS-G-3; it can be confirmed that FePNS-G-2 had the highest kinetic activity for ORR. Moreover, stability for ORR is an important factor. To analyze the stability of electrocatalysts, LSV curves were performed before and after 2000 cycles for both FePNS-G-2 and commercial 20% Pt/C in Fig. 5d. Fe-PNS-G-2 displayed a little decline after the 2000 cycles. However, benchmark 20% Pt/C showed considerable decline after the 2000 cycles. Besides, chronoamperometry performed for 10 h at the ORR potential in Fig. 5e. The relative current of FePNS-G-2 showed little decrease 89.62% after a 10-h CA measurement, suggesting excellent stability for ORR. Methanol tolerance is also critical to ORR catalysts. During the ORR process, methanol was injected into the electrolyte. After methanol is added, the original ORR current of Pt/C electrocatalyst dramatically changes, suggesting the incident of the methanol oxidation reaction, while the methanol chronoamperometric response of FePNS-G-2 recovers quickly upon the injection of methanol, suggesting good methanol tolerances in Fig. 5f. Carbon monoxide (CO) is

one of the important intermediates in the methanol oxidation process (MOR). CO is simply adsorbed on the surface of the metal material and affects the electrocatalyst performance. Therefore, it is required to conduct the CO-resistance poisoning performance of the catalyst [56]. Meanwhile, before and after 2000 cycles, the potential interval between OER and ORR of FePNS-G-2 and Pt/C + IrO_2 is shown in Fig. S9. These results show that the outstanding durability of FePNS-G-2 for both OER and ORR can serve as in the functional application in the Zn-air batteries.

Zn-air battery test for Fe-PNS-G-2 and benchmark Pt/C + IrO_2

To analyze the practical application of the air cathode as a catalyst, water-soluble Zn–air batteries (ZABs) were constructed. In Fig. 6a, the open-circuit potential (OCP) of Fe-PNS-G-2 was maintained for 500 s and 1.493 V (vs. Zn). This high value was close to the OCP of the theoretical Zn–air battery. As shown in Fig. 6b, the discharge polarization and the corresponding power density curve were performed. FePNS-G-2 has a higher power density of 168.3 mW cm^{-2} than FePNS-G-1 (49.2 mW cm^{-2}), FePNS-G-3 (132.5 mW cm^{-2}), and benchmark Pt/C + IrO_2 (142.8 mW cm^{-2}). The electrocatalytic performance of FePNS-G-2 and Pt/C + IrO_2 electrocatalyst was performed by charge and discharge polarization curves in Fig. 6c, which could be found that the Zn-air battery performance of FePNS-G-2 was more excellent than the benchmark Pt/C + IrO_2. As shown in Fig. 6d, during the discharging, the FePNS-G-2 cathode indicated a high specific capacitance of 782.36 mA h g^{-1}, which was almost utilization of theoretical capacitance about 820 mA h g^{-1}, whereas the benchmark Pt/C + IrO_2 cathode indicated a low specific capacitance of 769.88 mA h g^{-1}. To prove the rechargeable performance, the charge–discharge cycle test is consecutively performed in Fig. 6e. The initial discharge–charge voltage gap of FePNS-G-2 was only 0.9 V. However, the charge–discharge voltage gap of Pt/C + IrO_2 was more increased, suggesting these results have consistent stability in Figs. 4f and 5e. And the shape change after

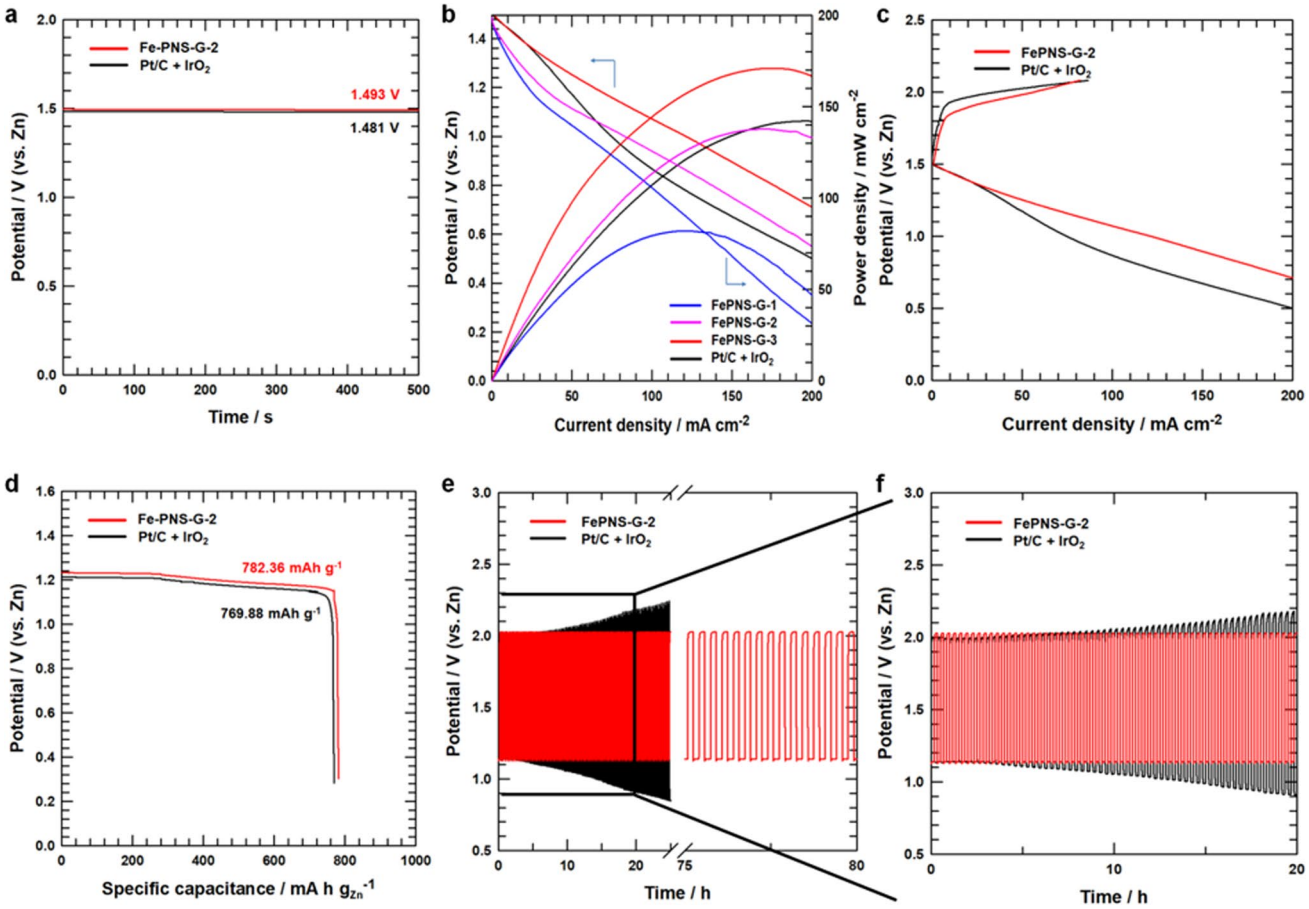

Fig. 6 **a** Open-circuit potential of FePNS-G-2 and benchmark Pt/C + IrO2. **b** Discharge polarization and corresponding power density of FePNS-G-1, FePNS-G-2, FePNS-G-3 and benchmark Pt/C + IrO2. **c** Charge and discharge polarizations of FePNS-G-2 and benchmark Pt/C + IrO2. **d** Specific capacitances of FePNS-G-2 and benchmark Pt/C + IrO2. **e** Charge and discharge cycle test of FePNS-G-2 and benchmark Pt/C + IrO2

2000 cycles test was examined by FE-TEM (Fig. S10). After 2000 cycles, the structure was preserved as porous structure on carbon substrate in FE-TEM, indicating structural stability. Excellent performance and cycle stability for charging discharging are key factors for applying electrocatalysts to rechargeable Zn-air battery. Therefore, FePNS-G-2 is a candidate electrocatalyst that is advantageous for functional applications of useful Zn-air battery.

Conclusion

In summary, we showed a controllable and easy synthesis of Fe, P, N, and S multidoped hierarchically open porous graphene (FePNS-G) using a simple method through calcination process. The annealing treatment temperature-dependent due to heteroatom doping was disclosed. FePNS-G-2 was contrasted with those of IrO_2 and Pt/C. FePNS-G displayed improved bifunctional activity sites in both OER and ORR activities, which is the charge and discharge reaction, respectively. The improvement is due to the porous structure of FePNS-G and the synergistic effects of Fe, P, N, and S multidoped in carbon. Moreover, The FePNS-G-2 electrocatalyst was an attractive candidate used as an air electrode in a high-density Zn-air batteries (ZABs) at a possible active site. FePNS-G-2 was tested with a catalyst for the ZABs, indicating that the potential gap between high stability after the charge–discharge cycles was lower than the $Pt/C + IrO_2$. The excellent electrochemical performance and cycle of the rechargeable ZABs with the Fe-PNS-G-2 cathode were encouraging for the energy conversion system and metal air batteries.

Supplementary Information The online version contains supplementary material available at https://doi.org/10.1007/s11581-022-04702-4.

Acknowledgements This research was supported by the Chung-Ang University Research Scholarship Grants in 2021 and also funded and conducted under the Competency Development Program for Industry Specialists of the Korean Ministry of Trade, Industry and Energy (MOTIE), operated by Korea Institute for Advancement of Technology (KIAT) (No. P0012453, Next-generation Display Expert Training Project for Innovation Process and Equipment, Materials Engineers).

References

1. Chu S, Majumdar A (2012) Opportunities and challenges for a sustainable energy future. Nature 488:294–303
2. Park D, Ju H, Kim J (2021) Enhanced thermoelectric properties of flexible N-type Ag2Se nanowire/polyvinylidene fluoride composite films synthesized via solution mixing, 93:333–338.
3. Kim M, Park J, Ju H, Kim JY, Cho H-S, Kim C-H, Kim B-H, Lee SW (2021) Understanding synergistic metal–oxide interactions of in situ exsolved metal nanoparticles on a pyrochlore oxide support for enhanced water splitting. Energ Environ Sci 14:3053–3063
4. Wang H-F, Tang C, Zhang Q (2018) A review of precious-metal-free bifunctional oxygen electrocatalysts: rational design and applications in Zn−air batteries. Adv Func Mater 28:1803329
5. Pan J, Xu YY, Yang H, Dong Z, Liu H, Xia BY (2018) Advanced architectures and relatives of air electrodes in Zn-air batteries. Adv Sci 5:1700691
6. Lee J-S, Tai Kim S, Cao R, Choi N-S, Liu M, Lee KT, Cho J (2011) Metal-air batteries with high energy density: Li-air versus Zn-air. Adv Energy Mater 1:34–50
7. Zhang Y, Deng Y-P, Wang J, Jiang Y, Cui G, Shui L, Yu A, Wang X, Chen Z (2021) Recent progress on flexible Zn-air batteries. Energy Storage Mater 35:538–549
8. Liu Q, Pan Z, Wang E, An L, Sun G (2020) Aqueous metal-air batteries: fundamentals and applications. Energy Storage Mater 27:478–505
9. He Y, Shang W, Ni M, Huang Y, Zhao H, Tan P (2022) In-situ observation of the gas evolution process on the air electrode of Zn-air batteries during charging. Chem Eng J 427:130862
10. Ma Y, Shang W, Yu W, Chen X, Xia W, Wang C, Tan P (2021) Synthesis of ultrasmall NiCo2O4 nanoparticle-decorated N-doped graphene nanosheets as an effective catalyst for Zn–air batteries. Energy Fuels 35:14188–14196
11. Tan P, Chen B, Xu H, Cai W, He W, Chen M, Ni M (2019) Synthesis of Fe2O3 Nanoparticle-Decorated N-doped reduced graphene oxide as an effective catalyst for Zn-air batteries. J Electrochem Soc 166:A616–A622
12. Kim K, Wie J, Kim J (2020) Synergistic interaction of P and N co-doping EDTA with controllable active EDTA-cobalt sites as efficient electrocatalyst for oxygen reduction reaction. J Ind Eng Chem 83:252–259
13. Kim M, Ju H, Kim J (2019) Single crystalline Bi2Ru2O7 pyrochlore oxide nanoparticles as efficient bifunctional oxygen electrocatalyst for hybrid Na-air batteries. Chem Eng J 358:11–19
14. Kim M, Ju H, Kim J (2018) Highly efficient bifunctional catalytic activity of bismuth rhodium oxide pyrochlore through tuning the covalent character for rechargeable aqueous Na–air batteries. J Mater Chem A 6:8523–8530
15. Lai C, Gong M, Zhou Y, Fang J, Huang L, Deng Z, Liu X, Zhao T, Lin R, Wang K, Jiang K, Xin H, Wang D (2020) Sulphur modulated Ni3FeN supported on N/S co-doped graphene boosts rechargeable/flexible Zn-air battery performance. Appl Catal B 274:119086
16. Liang S, Liang C (2019) High-density cobalt nanoparticles encapsulated with nitrogen-doped carbon nanoshells as a bifunctional catalyst for rechargeable zinc-air battery. Mater (Basel) 12:243
17. Gu L, Sun X-L, Zhao J, Gong B-Q, Bao Z-L, Jia H-L, Guan M-Y, Ma S-S (2021) A highly efficient bifunctional electrocatalyst (ORR/OER) derived from GO functionalized with carbonyl, hydroxyl and epoxy groups for rechargeable zinc–air batteries, New. J Chem 45:6535–6542
18. Masa J, Xia W, Sinev I, Zhao A, Sun Z, Grutzke S, Weide P, Muhler M, Schuhmann W (2014) Mn(x)O(y)/NC and Co(x)O(y)/NC nanoparticles embedded in a nitrogen-doped carbon matrix for high-performance bifunctional oxygen electrodes. Angew Chem Int Ed 53:8508–8512
19. Fu G, Cui Z, Chen Y, Li Y, Tang Y, Goodenough JB (2017) Ni3Fe-N doped carbon sheets as a bifunctional electrocatalyst for air cathodes. Adv Energy Mater 7:1601172
20. Lee DU, Park MG, Park HW, Seo MH, Ismayilov V, Ahmed R, Chen Z (2015) Highly active Co-doped LaMnO 3 perovskite oxide and N-doped carbon nanotube hybrid bi-functional catalyst for rechargeable zinc–air batteries. Electrochem Commun 60:38–41
21. Zhang J, Fu J, Song X, Jiang G, Zarrin H, Xu P, Li K, Yu A, Chen Z (2016) Laminated cross-linked nanocellulose/graphene oxide electrolyte for flexible rechargeable zinc-air batteries. Adv Energy Mater 6:1600476

22. Wang C, Li Z, Wang L, Niu X, Wang S (2019) Facile synthesis of 3D Fe/N codoped mesoporous graphene as efficient bifunctional oxygen electrocatalysts for rechargeable Zn–air batteries, ACS Sustain. Chem Eng 7:13873–13885
23. Jiang H, Yao Y, Zhu Y, Liu Y, Su Y, Yang X, Li C (2015) Iron carbide nanoparticles encapsulated in mesoporous Fe-N-doped graphene-like carbon hybrids as efficient bifunctional oxygen electrocatalysts. ACS Appl Mater Interfaces 7:21511–21520
24. Ambrosi A, Chua CK, Bonanni A, Pumera M (2014) Electrochemistry of graphene and related materials. Chem Rev 114:7150–7188
25. Cui W, Cheng N, Liu Q, Ge C, Asiri AM, Sun X (2014) Mo2C nanoparticles decorated graphitic carbon sheets: biopolymer-derived solid-state synthesis and application as an efficient electrocatalyst for hydrogen generation. ACS Catal 4:2658–2661
26. Chen WF, Wang CH, Sasaki K, Marinkovic N, Xu W, Muckerman JT, Zhu Y, Adzic RR (2013) Highly active and durable nanostructured molybdenum carbide electrocatalysts for hydrogen production, Energy Environ. Sci 6:943–951
27. Kim JY, Jang J-W, Youn DH, Magesh G, Lee JS (2014) A stable and efficient hematite photoanode in a neutral electrolyte for solar water splitting: towards stability engineering. Adv Energy Mater 4:1400476
28. Zhao R, Chen Y, Huang S (2021) Doping engineering on carbons as electrocatalysts for oxygen reduction reaction. Fundam Res 1:807–823
29. Zhang J, Zhang J, He F, Chen Y, Zhu J, Wang D, Mu S, Yang HY (2021) Defect and doping Co-engineered non-metal nanocarbon ORR electrocatalyst. Nanomicro Lett 13:65
30. Hu C, Dai L (2019) Doping of carbon materials for metal-free electrocatalysis. Adv Mater 31:1804672
31. Yang L, Shui J, Du L, Shao Y, Liu J, Dai L, Hu Z (2019) Carbon-based metal-free ORR electrocatalysts for fuel cells: past, present, and future. Adv Mater 31:1804799
32. Paraknowitsch JP, Thomas A (2013) Doping carbons beyond nitrogen: an overview of advanced heteroatom doped carbons with boron, sulphur and phosphorus for energy applications, Energy Environ. Sci 6:2839–2855
33. Li JC, Hou PX, Liu C (2017) Heteroatom-doped carbon nanotube and graphene-based electrocatalysts for oxygen reduction reaction. Small 13:1702002
34. Zhang J, Dai L (2015) Heteroatom-doped graphitic carbon catalysts for efficient electrocatalysis of oxygen reduction reaction. ACS Catal 5:7244–7253
35. Zhang J, Zhao Z, Xia Z, Dai L (2015) A metal-free bifunctional electrocatalyst for oxygen reduction and oxygen evolution reactions. Nat Nanotechnol 10:444–452
36. Tian G-L, Zhang Q, Zhang B, Jin Y-G, Huang J-Q, Su DS, Wei F (2014) Toward full exposure of "active sites": nanocarbon electrocatalyst with surface enriched nitrogen for superior oxygen reduction and evolution reactivity. Adv Funct Mater 24:5956–5961
37. Zheng Y, Chen S, Zhang KAI, Zhu J, Xu J, Zhang C, Liu T (2021) Ultrasound-triggered assembly of covalent triazine framework for synthesizing heteroatom-doped carbon nanoflowers boosting metal-free bifunctional electrocatalysis. ACS Appl Mater Interfaces 13:13328–13337
38. Li P, Wang H, Fan W, Huang M, Shi J, Shi Z, Liu S (2021) Salt assisted fabrication of lignin-derived Fe, N, P, S codoped porous carbon as trifunctional catalyst for Zn-air batteries and water-splitting devices. Chem Eng J 421:129704
39. Gao Z, Liu X, Zhang C, Ren Y (2022) Room-temperature seeded growth of tetraphenylphosphonium bromide single-crystalline fibers, cryst. Growth Des 22:2050–2057
40. Hu C, Dai L (2017) Multifunctional carbon-based metal-free electrocatalysts for simultaneous oxygen reduction, oxygen evolution, and hydrogen evolution. Adv Mater 29:1604942
41. Paudel DR, Pan UN, Singh TI, Gudal CC, Kim NH, Lee JH (2021) Fe and P doped 1T-phase enriched WS23D-dendritic nanostructures for efficient overall water splitting. Appl Catal B 286:119897
42. Tian GL, Zhao MQ, Yu D, Kong XY, Huang JQ, Zhang Q, Wei F (2014) Nitrogen-doped graphene/carbon nanotube hybrids: in situ formation on bifunctional catalysts and their superior electrocatalytic activity for oxygen evolution/reduction reaction. Small 10:2251–2259
43. Sun J, Lowe SE, Zhang L, Wang Y, Pang K, Wang Y, Zhong Y, Liu P, Zhao K, Tang Z, Zhao H (2018) Ultrathin nitrogen-doped holey carbon@graphene bifunctional electrocatalyst for oxygen reduction and evolution reactions in alkaline and acidic media. Angew Chem Int Ed 57:16511–16515
44. Chen Y, Wang H, Liu F, Gai H, Ji S, Linkov V, Wang R (2018) Hydrophobic 3D Fe/N/S doped graphene network as oxygen electrocatalyst to achieve unique performance of zinc-air battery. Chem Eng J 353:472–480
45. Chen Y, Huo S, Wang H (2018) Engineering morphology and porosity of N, S-doped carbons by ionothermal carbonisation for increased catalytic activity towards oxygen reduction reaction, Micro. Nano Lett 13:530–535
46. Wang L, Ambrosi A, Pumera M (2013) "Metal-free" catalytic oxygen reduction reaction on heteroatom- doped graphene is caused by trace metal impurities. Angew Chem Int Ed Engl 52:13818–13821
47. Chung MW, Choi CH, Lee SY, Woo SI (2015) Dimensionality-dependent oxygen reduction activity on doped graphene: is graphene a promising substrate for electrocatalysis? Nano Energy 11:526–532
48. Pampel J, Fellinger T-P (2016) Opening of bottleneck pores for the improvement of nitrogen doped carbon electrocatalysts. Adv Energy Mater 6:1502389
49. Wang B, Xu L, Liu G, Zhang P, Zhu W, Xia J, Li H (2017) Biomass willow catkin-derived Co3O4/N-doped hollow hierarchical porous carbon microtubes as an effective tri-functional electrocatalyst. J Mater Chem A 5:20170–20179
50. Gao Z, Liu X, Zhang C, Ren Y (2022) Room-temperature seeded growth of tetraphenylphosphonium bromide single-crystalline fibers. Cryst Growth Des 22:2050–2057
51. Zhao J, Liu Y, Quan X, Chen S, Zhao H, Yu H (2016) Nitrogen and sulfur co-doped graphene/carbon nanotube as metal-free electrocatalyst for oxygen evolution reaction: the enhanced performance by sulfur doping. Electrochim Acta 204:169–175
52. Liu K, Peng Z, Wang H, Ren Y, Liu D, Li J, Tang Y, Zhang N (2017) Fe3C@Fe/N doped graphene-like carbon sheets as a highly efficient catalyst in al-air batteries. J Electrochem Soc 6(164):475–483
53. Wu J, Zheng X, Jin C, Tian J, Yang R (2015) Ternary doping of phosphorus, nitrogen, and sulfur into porous carbon for enhancing electrocatalytic oxygen reduction. Carbon 92:327–338
54. Shao D, Li P, Zhang R, Zhao C, Wang D, Zhao C (2019) One-step preparation of Fe-doped Ni3S2/rGO@NF electrode and its superior OER performances. Int J Hydrog Energy 44:2664–2674
55. Gokhale R, Tsui L-K, Roach K, Chen Y, Hossen MM, Artyushkova K, Garzon F, Atanassov P (2018) Hydrothermal synthesis of platinum-group-metal-free catalysts: structural elucidation and oxygen reduction catalysis. ChemElectroChem 5:1848–1853
56. Wu N, Zhai M, Chen F, Zhang X, Guo R, Hu T, Ma M (2020) Nickel nanocrystal/nitrogen-doped carbon composites as efficient and carbon monoxide-resistant electrocatalysts for methanol oxidation reactions. Nanoscale 12:21687–21694